Squaring the circle – A curious phenomenon of fcc single crystals in spherical microindentation

B. Eidel *, F. Gruttmann

Institute of Materials and Mechanics in Civil-Engineering (IWMB), TU Darmstadt, Petersenstr. 12, D-64287 Darmstadt, Germany

Abstract

Spherical microindentation into the (0 0 1) surface of a FCC single crystal made of the Ni-base superalloy CMSX-4 has shown a remaining indent shape, that looks rather like a square than like a circle. In order to investigate this curious phenomenon, a digital surface model of the indentation crater is generated applying a backscatter electron detector along with digital image processing. The experimental measurings indicate a direction dependent pile-up accompanied by locally extended contact zones, which explains the squared shape of the spherical indent. Finite element simulations are conducted by means of a phenomenological orthotropic elasto-plasticity model within the framework of a multiplicative decomposition of the deformation gradient. The constitutive equations are formulated with respect to the isoclinic intermediate configuration. The simulation is in qualitative agreement with the experiment. Various rates of strain hardening in the simulation reveal the overlap of pile-up/sink-in with the direction dependent pile-up due to the crystal's anisotropy. The simulations predict that it is mainly the rate of strain hardening which shapes the anisotropy of the indentation topography.
© 2006 Elsevier B.V. All rights reserved.

1. Introduction

Indentation experiments play an ever more important role in materials science. They offer the possibility to understand the fundamental behaviour of solids and to extract material properties such as hardness, elastic moduli, yield strength and strain hardening parameters as well as to study fracture toughness, creep and temperature dependent properties. For a state-of-the-art review of the recent progress in instrumented indentation we refer to the articles in [1] and the references therein.

It is an important phenomenon of indentation experiments, that the material around the contact area tends to deform upwards, called pile-up, or downwards, called sink-in, with respect to the indented surface plane. The

formation of pile-up and sink-in topographies in isotropic materials has been shown to be primarily driven by the strain–hardening potential of the indented material, [2–5]. These studies have revealed that the surface around the indents tends to pile up against the indenter in the case that the indented material has only little potential to strain–harden, e.g., as the sample is heavily pre-strained. By contrast, in well annealed metals, that exhibit a high strain–hardening capacity, the material tends to sink in at the surface level. As a consequence of pile-up or sink-in, large differences may arise between the true contact area and the apparent contact area [4], which affects the determination of mechanical properties such as hardness; for a discussion corroborated on finite element simulations, see [3].

The present contribution is focused on a curious phenomenon of fcc single crystals in spherical microindentation. In an experiment within SFB 298, a special collaborative research centre at TU Darmstadt, it was

---

* Corresponding author. Tel.: +49 6151 16 2439; fax: +49 6151 16 2338.
  E-mail address: eidel@iwmb.tu-darmstadt.de (B. Eidel).

observed, that a *ball*, after being indented into a (0 0 1) oriented single-crystal sample of fcc-structure, left the lasting impression shown in the photograph of Fig. 1, [6], which gives rise to the term *squaring the circle*. As it turned out, this phenomenon was already reported in literature; Dyer [7] performed experiments of ball indentation on the (0 0 1) face of fcc copper, where he observed a squared shape of the indentation at the surface. A study on spherical microindentation on (1 0 0), (1 1 0) and (1 1 1) oriented NiAl and its corresponding anisotropic surface topographies around the indents is reported in [8]. In [9] orientation dependent pile-up patterns and microtextures in conical nanoindentation into copper single crystals are investigated. A crystal plasticity model predicts within finite-element simulations the observed deformation patterns for different orientations of the crystal.

The contribution of the present paper, based on [10], can be summarized as follows:

(i) On the experimental side, a digital surface model of the indentation crater is reconstructed by means of an image processing software. Image data of scanning electron microscopy (SEM) along with a backscatter electron detector (BSD) serve as input in this process. The reconstructed surface indicates a strongly direction dependent pile-up pattern accompanied by a locally extended contact area, which causes the *squaring of the circle*. This observation and the discrete slip-traces at the surface can be explained by specific plastic glide in the fcc single crystal.

(ii) On the modelling side, the main characteristics of a phenomenological model for orthotropic elasto-plasticity within the framework of continuum mechanics with internal state variables are outlined. The constitutive equations, i.e. the elasticity law and the quadratic yield condition in terms of the Mandel stress tensor, are formulated with respect to the isoclinic configuration according to a multiplicative decomposition of the deformation gradient.

(iii) Finite element simulations demonstrate the influence of the strain–hardening rate on the deformation topography and its overlap with the observed aniso-
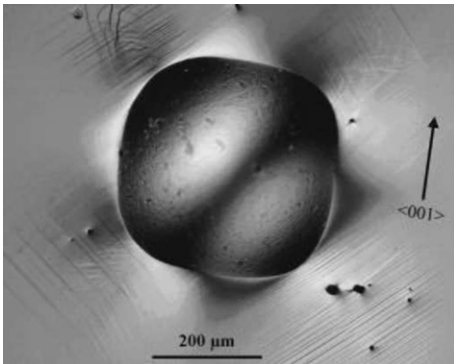
tropic effect of direction-dependent pile-up. New predictions are achieved in the present analysis, how these two different effects overlap.

2. Thermodynamical framework for anisotropic elasto-plasticity

Motivated by a micromechanical view of elasto-plastic deformations in crystals, a multiplicative decomposition of the deformation gradient $\mathbf{F}$ is assumed to hold:

$$\mathbf{F} = \mathbf{F}^e \mathbf{F}^p = \mathbf{F}^e \mathbf{\Phi} \widetilde{\mathbf{F}}^p, \tag{1}$$

where $\mathbf{F}^e$ is the elastic part and $\mathbf{F}^p$ the plastic part, that introduces a plastic intermediate configuration $\widehat{\mathsf{R}}_t$. The orthogonal tensor $\mathbf{\Phi}$ rotates some characteristic anisotropy axes from the so-called isoclinic configuration $\widetilde{\mathsf{R}}_t$ to $\widehat{\mathsf{R}}_t$. For original references dealing with the decompositions in (1) see [11–13]. In the sequel the second law of thermodynamics is formulated with respect to $\widehat{\mathsf{R}}_t$. A law of hyper-elasticity and the internal dissipation inequality are obtained with respect to $\widetilde{\mathsf{R}}_t$ and $\widehat{\mathsf{R}}_t$, where in the latter configuration the constitutive equations of the present work are formulated. For that aim we introduce plastic velocity gradients $\widehat{\mathbf{L}}^p$ and $\widetilde{\mathbf{L}}^p$ for $\mathbf{F}^p$ and $\widetilde{\mathbf{F}}^p$, their decomposition in symmetric and skew-symmetric parts and the relations among them:

$$\widetilde{\mathbf{L}}^p = \dot{\widetilde{\mathbf{F}}}^p \widetilde{\mathbf{F}}^{p-1} = \widetilde{\mathbf{D}}^p + \widetilde{\mathbf{W}}^p = \mathbf{\Phi}^T \left(\widehat{\mathbf{L}}^p - \dot{\mathbf{\Phi}} \mathbf{\Phi}^T \right) \mathbf{\Phi}, \tag{2}$$

$$\widehat{\mathbf{L}}^p = \dot{\mathbf{F}}^p \mathbf{F}^{p-1} = \widehat{\mathbf{D}}^p + \widehat{\mathbf{W}}^p = \dot{\mathbf{\Phi}} \mathbf{\Phi}^T + \mathbf{\Phi} \widetilde{\mathbf{L}}^p \mathbf{\Phi}^T. \tag{3}$$

Following Dafalias, [14], we call the difference of spin tensors

$$\widehat{\mathbf{\Omega}} = \widehat{\mathbf{W}}^p - \dot{\mathbf{\Phi}} \mathbf{\Phi}^T \tag{4}$$

the plastic spin, $\dot{\mathbf{\Phi}} \mathbf{\Phi}^T$ the constitutive spin of an underlying substructure (lattice spin in crystal plasticity) and $\widehat{\mathbf{W}}^p$ the plastic material spin. The constitutive equations are restricted by the second law in the form of the Clausius–Duhem-inequality, which reads under the assumption of isothermal deformations with uniform temperature distribution in the plastic intermediate configuration, [15],

$$\widehat{\mathsf{R}}_t : \quad \mathscr{D} = \widehat{\mathbf{S}} : \overset{\triangle}{\widehat{\mathbf{E}}} - \dot{\Psi} \geqslant 0, \tag{5}$$

where $\widehat{\mathbf{S}}$ is the Second Piola–Kirchhoff stress tensor and

$$\overset{\triangle}{\widehat{\mathbf{E}}} = \dot{\widehat{\mathbf{E}}} + \widehat{\mathbf{L}}^{pT} \widehat{\mathbf{E}} + \widehat{\mathbf{E}} \widehat{\mathbf{L}}^p = \overset{\triangle}{\widehat{\mathbf{E}}}{}^e + \overset{\triangle}{\widehat{\mathbf{E}}}{}^p = \overset{\triangle}{\widehat{\mathbf{E}}}{}^e + \widehat{\mathbf{D}}^p \tag{6}$$

is the lower Oldroyd rate of the Green–Lagrangian strain tensor $\widehat{\mathbf{E}}$ in $\widehat{\mathsf{R}}_t$. $\dot{\Psi}$ denotes the material time derivative of the free energy function. For Ψ an additive decomposition into an elastic part Ψ^e and a plastic part Ψ^p for isotropic hardening is assumed to hold, $\Psi = \Psi^e + \Psi^p$. Inserting (6) and the decomposition of Ψ into (5), yields

$$\widehat{\mathsf{R}}_t : \quad \mathscr{D} = \widehat{\mathbf{S}} : \dot{\widehat{\mathbf{E}}}{}^e + \widehat{\mathbf{\Sigma}} : \widehat{\mathbf{L}}^p - \dot{\Psi} \geqslant 0, \tag{7}$$

where $\widehat{\mathbf{\Sigma}} = (2\widehat{\mathbf{E}}{}^e + \mathbf{1})\widehat{\mathbf{S}}$ is the so-called Mandel stress tensor, [16], which is for anisotropic elasticity in general

Fig. 1. Squared round shape of a (0 0 1) oriented fcc single crystal in spherical indentation, optical light microscopy [6].

nonsymmetric. Inserting the time derivative $\dot{\Psi}^{\mathrm{e}}$ into (5) yields, after some algebra,

$$\left(\widehat{\mathbf{S}} - \boldsymbol{\Phi}\frac{\partial\Psi^{\mathrm{e}}}{\partial\widetilde{\mathbf{E}}^{\mathrm{e}}}\boldsymbol{\Phi}^{T}\right):\dot{\widehat{\mathbf{E}}}^{\mathrm{e}} + \widehat{\boldsymbol{\Sigma}}:\widehat{\mathbf{L}}^{\mathrm{p}}$$

$$- \left(2\widehat{\mathbf{E}}^{\mathrm{e}}\boldsymbol{\Phi}\frac{\partial\Psi^{\mathrm{e}}}{\partial\widetilde{\mathbf{E}}^{\mathrm{e}}}\boldsymbol{\Phi}^{T}\right):\dot{\boldsymbol{\Phi}}\boldsymbol{\Phi}^{T} - \dot{\Psi}^{\mathrm{p}} \geqslant 0. \qquad (8)$$

Applying standard arguments in rational thermodynamics, a law of hyperelasticity is obtained in $\widehat{\mathsf{R}}_t$ and $\widetilde{\mathsf{R}}_t$

$$\widehat{\mathbf{S}} = \boldsymbol{\Phi}\frac{\partial\widetilde{\Psi}^{\mathrm{e}}\left(\widetilde{\mathbf{E}}^{\mathrm{e}}\right)}{\partial\widetilde{\mathbf{E}}^{\mathrm{e}}}\boldsymbol{\Phi}^{T}, \qquad \widetilde{\mathbf{S}} = \frac{\partial\widetilde{\Psi}^{\mathrm{e}}\left(\widetilde{\mathbf{E}}^{\mathrm{e}}\right)}{\partial\widetilde{\mathbf{E}}^{\mathrm{e}}}, \qquad (9)$$

where $\widetilde{\mathbf{E}}^{\mathrm{e}} = \boldsymbol{\Phi}^{T}\widehat{\mathbf{E}}^{\mathrm{e}}\boldsymbol{\Phi}$ and $\widehat{\mathbf{S}} = \boldsymbol{\Phi}\widetilde{\mathbf{S}}\boldsymbol{\Phi}^{T}$. Assuming that the law of hyperelasticity also holds for plastic deformation processes, the internal dissipation inequality is obtained in $\widehat{\mathsf{R}}_t$ and by pull-back via $\boldsymbol{\Phi}$ in $\widetilde{\mathsf{R}}_t$:

$$\widehat{\mathsf{R}}_t: \quad \mathscr{D}_{\mathrm{int}} = \widehat{\boldsymbol{\Sigma}}:\left(\widehat{\mathbf{L}}^{\mathrm{p}} - \dot{\boldsymbol{\Phi}}\boldsymbol{\Phi}^{T}\right) - \dot{\Psi}^{\mathrm{p}}$$
$$\widetilde{\mathsf{R}}_t: \qquad = \widetilde{\boldsymbol{\Sigma}}:\widetilde{\mathbf{L}}^{\mathrm{p}} - \dot{\Psi}^{\mathrm{p}} \geqslant 0, \qquad (10)$$

where $\widetilde{\boldsymbol{\Sigma}} = (2\widetilde{\mathbf{E}}^{\mathrm{e}} + \mathbf{1})\widetilde{\mathbf{S}}$ is the Mandel stress tensor in $\widetilde{\mathsf{R}}_t$. In [15] a normality rule for the deformation rate $\widehat{\mathbf{L}}^{\mathrm{p}} - \dot{\boldsymbol{\Phi}}\boldsymbol{\Phi}^{T}$ is derived as a sufficient condition for the so-called postulate of Il'iushin. In the present approach, a normality rule is formulated with respect to $\widetilde{\mathsf{R}}_t$

$$\widetilde{\mathbf{L}}^{\mathrm{p}} = \widetilde{\mathbf{D}}^{\mathrm{p}} + \widetilde{\mathbf{W}}^{\mathrm{p}} = \lambda\left(\frac{\partial\Phi}{\partial\widetilde{\boldsymbol{\Sigma}}_{\mathrm{s}}} + \frac{\partial\Phi}{\partial\widetilde{\boldsymbol{\Sigma}}_{\mathrm{a}}}\right) := \lambda\left(\widetilde{\mathbf{N}}_{\mathrm{s}} + \widetilde{\mathbf{N}}_{\mathrm{a}}\right), \qquad (11)$$

where the tensor valued function $\widetilde{\mathbf{N}} = \widetilde{\mathbf{N}}_{\mathrm{s}} + \widetilde{\mathbf{N}}_{\mathrm{a}}$ is directed along the outward normal on the yield surface $\Phi = 0$. The scalar λ is the plastic multiplier, $\lambda \geqslant 0$. The yield function Φ is assumed to depend on the symmetric part of $\widetilde{\boldsymbol{\Sigma}}$, $\Phi = \widetilde{\Phi}(\widetilde{\boldsymbol{\Sigma}}_{\mathrm{s}})$, which results in $\widetilde{\mathbf{W}}^{\mathrm{p}} = \mathbf{0}$. Since $\widetilde{\mathbf{W}}^{\mathrm{p}} = \boldsymbol{\Phi}^{T}(\widehat{\mathbf{W}}^{\mathrm{p}} - \dot{\boldsymbol{\Phi}}\boldsymbol{\Phi}^{T})\boldsymbol{\Phi} = \boldsymbol{\Phi}^{T}\widehat{\boldsymbol{\Omega}}\boldsymbol{\Phi}$, see Eq. (2), it follows, that in $\widehat{\mathsf{R}}_t$ the plastic spin vanishes, $\widehat{\boldsymbol{\Omega}} = \mathbf{0}$. Thus, the plastic material spin equals the constitutive spin, $\widehat{\mathbf{W}}^{\mathrm{p}} = \dot{\boldsymbol{\Phi}}\boldsymbol{\Phi}^{T}$.

2.1. Invariant representation of orthotropic elasto-plasticity

For the simulation of the indentation test into the fcc single crystal, cubic symmetry is treated as a special case of orthotropy. The elastic free energy function Ψ^{e} and the yield function Φ are assumed to obey an invariant representation as isotropic tensor functions, see e.g., [17–19]. The group of symmetry transformations $\mathscr{G}_{\mathrm{ortho}}$ for orthotropic materials is defined in $\widetilde{\mathsf{R}}_t$ by

$$\mathscr{G}_{\mathrm{ortho}} = \{\mathbf{R}^{\pi}_{1\tilde{\mathbf{m}}}, \ \mathbf{R}^{\pi}_{2\tilde{\mathbf{m}}}, \ \mathbf{R}^{\pi}_{3\tilde{\mathbf{m}}}, \pm\mathbf{1}\}, \qquad (12)$$

where $\mathbf{R}^{\pi}_{i\tilde{\mathbf{m}}}, i = 1, 2, 3$ denotes a rotation around direction $^{i}\tilde{\mathbf{m}}$ by angle π; the identity $+\mathbf{1}$ and the central inversion $-\mathbf{1}$ are symmetry transformations of every isotropy group. The so-called structural tensors are introduced:

$$^{1}\widetilde{\mathbf{M}} := {}^{1}\tilde{\mathbf{m}} \otimes {}^{1}\tilde{\mathbf{m}}, \quad {}^{2}\widetilde{\mathbf{M}} := {}^{2}\tilde{\mathbf{m}} \otimes {}^{2}\tilde{\mathbf{m}} \quad \text{and}$$
$$^{3}\widetilde{\mathbf{M}} := {}^{3}\tilde{\mathbf{m}} \otimes {}^{3}\tilde{\mathbf{m}}, \quad |{}^{i}\tilde{\mathbf{m}}| = 1, \qquad (13)$$

which reflect the orthotropic material symmetry in the sense that they are invariant with respect to transformations of the symmetry group $\mathscr{G}_{\mathrm{ortho}}$. For $\sum_{i=1}^{3}{}^{i}\widetilde{\mathbf{M}} = \mathbf{1}$ we may discard $^{3}\widetilde{\mathbf{M}}$ from the set of structural tensors. The integrity basis for Ψ^{e} contains invariants in terms of $\widetilde{\mathbf{E}}^{\mathrm{e}} = \boldsymbol{\Phi}^{T}\widehat{\mathbf{E}}^{\mathrm{e}}\boldsymbol{\Phi}$, $^{1}\widetilde{\mathbf{M}}$ and $^{2}\widetilde{\mathbf{M}}$:

$$J_1 := \mathrm{tr}\left[\widetilde{\mathbf{E}}^{\mathrm{e}}\right], \quad J_2 := \mathrm{tr}\left[(\widetilde{\mathbf{E}}^{\mathrm{e}})^2\right], \quad J_3 := \mathrm{tr}\left[(\widetilde{\mathbf{E}}^{\mathrm{e}})^3\right], \quad J_4 := \mathrm{tr}\left[{}^{1}\widetilde{\mathbf{M}}\widetilde{\mathbf{E}}^{\mathrm{e}}\right],$$

$$J_5 := \mathrm{tr}\left[{}^{1}\widetilde{\mathbf{M}}(\widetilde{\mathbf{E}}^{\mathrm{e}})^2\right], \quad J_6 := \mathrm{tr}\left[{}^{2}\widetilde{\mathbf{M}}\widetilde{\mathbf{E}}^{\mathrm{e}}\right], \quad J_7 := \mathrm{tr}\left[{}^{2}\widetilde{\mathbf{M}}(\widetilde{\mathbf{E}}^{\mathrm{e}})^2\right],$$
$$(14)$$

where $\mathrm{tr}[\bullet]$ denotes the trace of a second order tensor. For Ψ^{e} a quadratic form is assumed to hold

$$\widetilde{\Psi}^{\mathrm{e}}(\widetilde{\mathbf{E}}^{\mathrm{e}}, {}^{1}\widetilde{\mathbf{M}}, {}^{2}\widetilde{\mathbf{M}}) = \frac{1}{2}\lambda J_1^2 + \mu J_2 + (\alpha_1 J_4 + \alpha_2 J_6)J_1$$

$$+ 2\mu_1 J_5 + 2\mu_2 J_7 + \frac{1}{2}\beta_1 J_4^2$$

$$+ \frac{1}{2}\beta_2 J_6^2 + \beta_3 J_4 J_6, \qquad (15)$$

where λ, μ, μ_1, μ_2, α_1, α_2, β_1, β_2, β_3 represent material parameters. Differentiation yields explicit expressions for the Second Piola–Kirchhoff stress tensor $\widetilde{\mathbf{S}} = \partial_{\widetilde{\mathbf{E}}^{\mathrm{e}}}\Psi^{\mathrm{e}}$ and the elasticity tensor $\mathbb{C}^{\mathrm{e}} = \partial^2_{\widetilde{\mathbf{E}}^{\mathrm{e}}\widetilde{\mathbf{E}}^{\mathrm{e}}}\Psi^{\mathrm{e}}$.

The orthotropic yield function Φ is chosen to be quadratic in $\mathrm{dev}\widetilde{\boldsymbol{\Sigma}}_{\mathrm{s}}$, where the deviator ensures plastic incompressibility, $\det\widetilde{\mathbf{F}}^{p} = 1$, if an associative flow-rule is adopted. In analogy to Ψ^{e}, we choose for the yield function a representation as an isotropic tensor function:

$$\Phi = \widetilde{\Phi}(\mathrm{dev}\widetilde{\boldsymbol{\Sigma}}_{\mathrm{s}}, {}^{1}\widetilde{\mathbf{M}}, {}^{2}\widetilde{\mathbf{M}}). \qquad (16)$$

The integrity basis in terms of $\mathrm{dev}\widetilde{\boldsymbol{\Sigma}}_{\mathrm{s}}$ and the structural tensors $^{1}\widetilde{\mathbf{M}}$ and $^{2}\widetilde{\mathbf{M}}$, is given by

$$I_1 := \mathrm{tr}\left[\left(\mathrm{dev}\widetilde{\boldsymbol{\Sigma}}_{\mathrm{s}}\right)^2\right], \quad I_2 := \mathrm{tr}\left[{}^{1}\widetilde{\mathbf{M}}\left(\mathrm{dev}\widetilde{\boldsymbol{\Sigma}}_{\mathrm{s}}\right)^2\right],$$

$$I_3 := \mathrm{tr}\left[{}^{2}\widetilde{\mathbf{M}}\left(\mathrm{dev}\widetilde{\boldsymbol{\Sigma}}_{\mathrm{s}}\right)^2\right], \quad I_4 := \mathrm{tr}\left[{}^{1}\widetilde{\mathbf{M}}\mathrm{dev}\widetilde{\boldsymbol{\Sigma}}_{\mathrm{s}}\right],$$

$$I_5 := \mathrm{tr}\left[{}^{2}\widetilde{\mathbf{M}}\mathrm{dev}\widetilde{\boldsymbol{\Sigma}}_{\mathrm{s}}\right], \quad I_6 := \mathrm{tr}\left[\left(\mathrm{dev}\widetilde{\boldsymbol{\Sigma}}_{\mathrm{s}}\right)^3\right]. \qquad (17)$$

In view of a quadratic yield criterion, the cubic invariant I_6 is discarded, yielding

$$\Phi = \eta_1 I_1 + \eta_2 I_2 + \eta_3 I_3 + \eta_4 I_4^2 + \eta_5 I_5^2 + \eta_6 I_4 I_5 - \left(1 + \frac{\hat{\xi}(\mathrm{e}^{\mathrm{p}})}{Y_{11}^{0}}\right)^2. \qquad (18)$$

Here, the scalars $\eta_i | i = 1, \ldots, 6$ are material parameters, which can be related to physical normal yield stresses Y_{11}, Y_{22}, Y_{33} and shear yield stresses Y_{12}, Y_{13}, Y_{23}. The scalar-valued variable $\xi = \hat{\xi}(\mathrm{e}^{\mathrm{p}})$ models isotropic hardening in terms of the equivalent plastic strain e^{p}, defined by $\dot{\mathrm{e}}^{\mathrm{p}} = \sqrt{2/3}\|\widetilde{\mathbf{D}}^{\mathrm{p}}\|$. The constitutive model for orthotropic elasto-plasticity is summarized in (19).

Kinematics	$\mathbf{F} = \mathbf{F}^e \mathbf{F}^p = \mathbf{F}^e \boldsymbol{\Phi} \widetilde{\mathbf{F}}^p$
	$\widetilde{\mathbf{L}}^p = \dot{\widetilde{\mathbf{F}}}^p \widetilde{\mathbf{F}}^{p-1} = \widetilde{\mathbf{D}}^p + \widetilde{\mathbf{W}}^p$
Free energy	$\Psi = \widetilde{\Psi}^e \left(\widetilde{\mathbf{E}}^e, {}^1\widetilde{\mathbf{M}}, {}^2\widetilde{\mathbf{M}} \right) + \widetilde{\Psi}^{p,\mathrm{iso}}(e^p)$
Elasticity law	$\widetilde{\mathbf{S}} = \dfrac{\partial \Psi^e}{\partial \widetilde{\mathbf{E}}^e}, \widetilde{\boldsymbol{\Sigma}} = \widetilde{\mathbf{C}}^e \widetilde{\mathbf{S}}$
Yield function	$\Phi = \widetilde{\Phi} \left(\mathrm{dev}\widetilde{\boldsymbol{\Sigma}}_s, {}^1\widetilde{\mathbf{M}}, {}^2\widetilde{\mathbf{M}}, \xi \right)$
Isotropic hardening	$\xi = \dfrac{\partial \Psi^{p,\mathrm{iso}}}{\partial e^p} = k \cdot e^p$
Associative flow rule	$\widetilde{\mathbf{D}}^p = \lambda \dfrac{\partial \Phi}{\partial \widetilde{\boldsymbol{\Sigma}}_s} := \lambda \widetilde{\mathbf{N}}$
Evolution of e^p	$\dot{e}^p = \sqrt{\dfrac{2}{3}} \|\widetilde{\mathbf{D}}^p\|$
Optimization conditions	$\lambda \geqslant 0, \ \Phi \leqslant 0, \ \lambda\Phi = 0$

$$(19)$$

3. Spherical indentation

3.1. 3D-experimental investigation

The material in the indentation test, CMSX-4, is a two-phase material, where semicoherent, ordered Ni_3Al precipitates of $L1_2$ type (γ'-phase) are embedded in a Ni-matrix of fcc structure (γ-phase). The volume fraction of the precipitates is ≈ 70 %. Since the mean contact diameter in the indentation experiment $\bar{d} \approx 400\,\mu m$ is much larger than the size of a single precipitate $d_p < 1\,\mu m$, it is assumed that the material therefore exhibits a rather homogenized response concerning the overall deformation behaviour, where the two-phase composition can be neglected in modelling. The 3D-reconstruction of the indentation imprint from BSD images was realized by advanced algorithms for image processing in the software system MeX of alic-ona. The results reveal the formation of four distinct pile-up hillocks at $\langle 110 \rangle$ directions, which reflects the material's four-fold symmetry of the fcc-crystal in the plane of indentation, Fig. 2(a). A comparison of the isolines of height in Fig. 2(a) with the photograph in Fig. 1 elucidates, that from bird's eye view those hillocks appear as *corners* of a square deviating from the circular shape: a kind of *squaring the circle*.

A refined profile-analysis of the Brinell-imprint is obtained by cross-sectional views, displayed in Fig. 3. The profiles (III) and (IV) representing cuts in $\langle 110 \rangle$ directions each indicate the formation of hillocks due to strong pile-up. The peaks of these hillocks are acute and it can be concluded, that they precisely mark the edge of the contact area between indenter and sample. The peaks are well above the initial surface plane, between 15 μm and 20 μm. The maximum height of the profile peak above the center of indentation amounts to 53 μm.

These properties are in contrast to the $\langle 100 \rangle$ cuts, profiles (I) and (II), where only a weak upheaval of $\approx 5\,\mu m$ above the initial surface plane is observed. Besides this, the transition from the inside of the indent to the outside parts is smooth.

Different amount of pile-up results in different extensions of the contact area, i.e. diameters in $\langle 100 \rangle$ directions and in $\langle 110 \rangle$ directions. Two different readings for each pair of crystallographic equivalent directions resulted in the mean diameters $d_{\langle 100 \rangle} \approx 370\,\mu m$ and $d_{\langle 110 \rangle} \approx 420\,\mu m$. The ratio of the mean contact radius a divided by the tip radius $R = 625\,\mu m$ is $a/R = 0.316$.

The pile-up pattern formation can be understood as a result of a crystallographic governed process. Both, pile-up at $\langle 110 \rangle$ directions and the emergence of discrete slip traces at the surface, best seen at the bottom right in Fig. 1, indicate, that the active glide systems in the fcc single crystal mainly consist of octahedral $\{111\}$ glide planes with $\langle 110 \rangle$ slip directions. A $(1\bar{1}1)$ slip plane intersects the indented (001) surface along the $[110]$ direction, a (111) slip plane intersects the (001) surface at the $[1\bar{1}0]$ direction. This observation is in agreement with the findings in the early work of Dyer [7] and with [9].
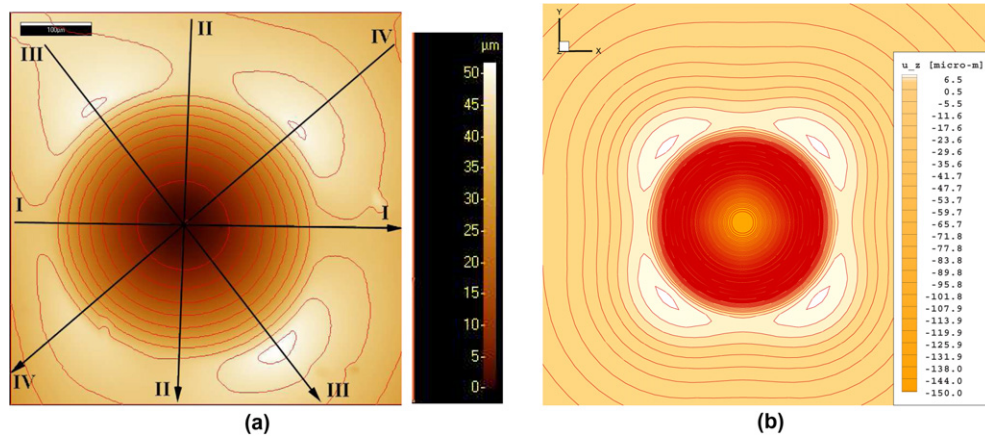

Fig. 2. Isolines of height, u_z [μm], of the indentation crater: (a) in the experiment, (b) in the simulation for $k = 10$ GPa. The peaks of the four hillocks, in white color, denote the boundary of the contact area in $\langle 110 \rangle$ directions. They appear as corners in Fig. 1, leading to a squared shape of the indentation.
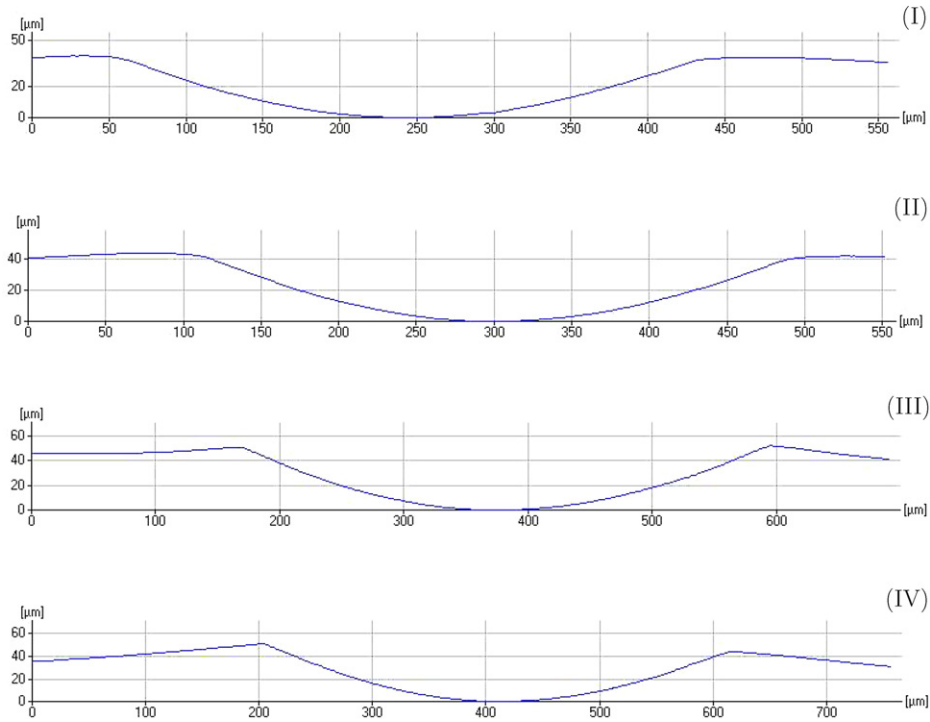
Fig. 3. Profiles of spherical-indentation. The four cross-sections (I)–(IV) from left to right correspond to the four cuts in the direction of the arrows displayed in Fig. 2 (a). (I) and (II) are $\langle 1\,0\,0\rangle$ cuts, (III) and (IV) are $\langle 1\,1\,0\rangle$ cuts.

3.2. Simulation versus experiment

The finite element simulations are conducted by means of a Q1A3E5 8-node brick element, [20]. The backward Euler algorithm is employed for the time integration of the evolution laws. For the extension of the halfspace the radius $r = 2.5$ mm and the thickness $t = 2.5$ mm are chosen in the simulations. The non-uniform discretization with 6400 elements reflects the region of indentation exhibiting large gradients in the deformations, Fig. 4. A unilateral contact formulation along with the penalty-method is applied for the simulations, where the ball-indenter made of hardened steel with diameter $D = 1.25$ mm is considered to be rigid. Table 1 summarizes the material data of CMSX-4 used in the simulations. The elastic constants
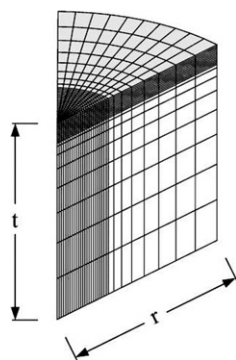
Table 1
Material data of CMSX-4 in the simulations

Elastic moduli	$c_{11}/c_{12}/c_{44}$	244/154/129 GPa
Normal yield stress	$Y_{11} = Y_{22} = Y_{33}$	820 MPa
Shear yield stress	$Y_{12} = Y_{13} = Y_{23}$	660 MPa
Hardening modulus	k	0/5/10/20 GPa
Anisotropy axes	$^{1}\tilde{\mathbf{m}}, \,^{2}\tilde{\mathbf{m}}$	$[1,0,0]^{T}, [0,1,0]^{T}$

are taken from [6]. For the plastic behaviour the experimental data of the proportional limits $R_{p0.2\langle 0\,0\,1\rangle} = 820$ MPa and $R_{p0.2\langle 1\,1\,1\rangle} = 1130$ MPa in [6] are adapted to the specific format of the yield condition used here. In a simple tension test in $[1\,1\,1]$-direction with one finite element the normal yield stresses are set to $Y_{11} = Y_{22} = Y_{33} = R_{p0.2\langle 0\,0\,1\rangle}$ and the unknown shear yield stresses $Y_{12} = Y_{13} = Y_{23}$ are iteratively determined by the requirement of the onset of plastic yielding at $R_{p0.2\langle 1\,1\,1\rangle}$. This yields the value of the shear yield stress in Table 1. As can be seen in Fig. 2, simulation (b) and experiment (a) are in qualitative agreement with respect to the formation of pile-up in $\langle 1\,1\,0\rangle$ directions. The ratio of the maximum pile-up to the indentation depth is 0.39 in the experiment; in the simulations this ratio is throughout much smaller, depending on the hardening rate; for $k = 0$ GPa it is 0.23, for $k > 0$ GPa it constantly decreases, for $k = 20$ GPa it is approximately zero, since absolute pile-up vanishes. This quantitative gap between experiment and simulation is a point of further research work. The focus in the present study is on the qualitative deformation behaviour and the influence of the hardening rate. It is worth to note that

Fig. 4. Finite element discretization of an eighth of the halfspace, exploiting four cubic symmetry planes.

the used material model cannot describe the deformation pattern for the indentation in (1 1 1)- and (1 1 0)-directions with its six-fold and four-fold symmetry as reported in [9].

3.3. Simulation – pattern formation in indentation topography

The guiding interest in the simulations is: How does the experimentally observed anisotropic effect of direction-dependent pile-up overlaps with the well-known effect of strain–hardening to cause sink-in ? Data of the real strain–hardening capacity of the tested CMSX-4 sample at room temperature were not available. In order to answer the above question the simulations are conducted for different parameters k in linear isotropic hardening, $k = 0$; 5; 10; 20 GPa, where the (0 0 1) orientation of the surface is kept fixed. Fig. 5 shows the isolines of height of the remaining deformation patterns upon unloading. In order to highlight merely the anisotropic deviations from the isotropic circular indentation shape, ranges of into-depth displacements with circular isolines of height are cut-off in the legends.

For zero hardening, $k = 0$ GPa, the surface exhibits the formation of pile-up all around the indentation crater, which attains close to the craters rim approximately constant height in circumferential direction, Fig. 5(a). There, pile-up is isotropic. At larger radial distance, pile-up exhibits weak maxima in ⟨1 1 0⟩ directions, where a corner-formation is observable, i.e., the isolines of height show locally a higher curvature. Generally, for $k = 0$ GPa the material's cubic symmetry in the indented (0 0 1) plane is only weakly reflected in the deformation pattern.

With increasing strain hardening capacity two trends are observable:

First, the profiles of pile-up increasingly differentiate in different directions, which means, that in ⟨1 1 0⟩ directions distinct hillocks emerge, which are each separated by valleys, Fig. 5, from (a) to (d). The conclusion is, that isotropic hardening drives the anisotropy of pattern formation. Second, the overall pile-up for zero hardening $k = 0$ GPa continuously changes to sink-in. These two effects overlap. The formation of local pile-up is overlapped by sink-in and for the largest value of isotropic hardening considered here, $k = 20$ GPa, it is even overruled
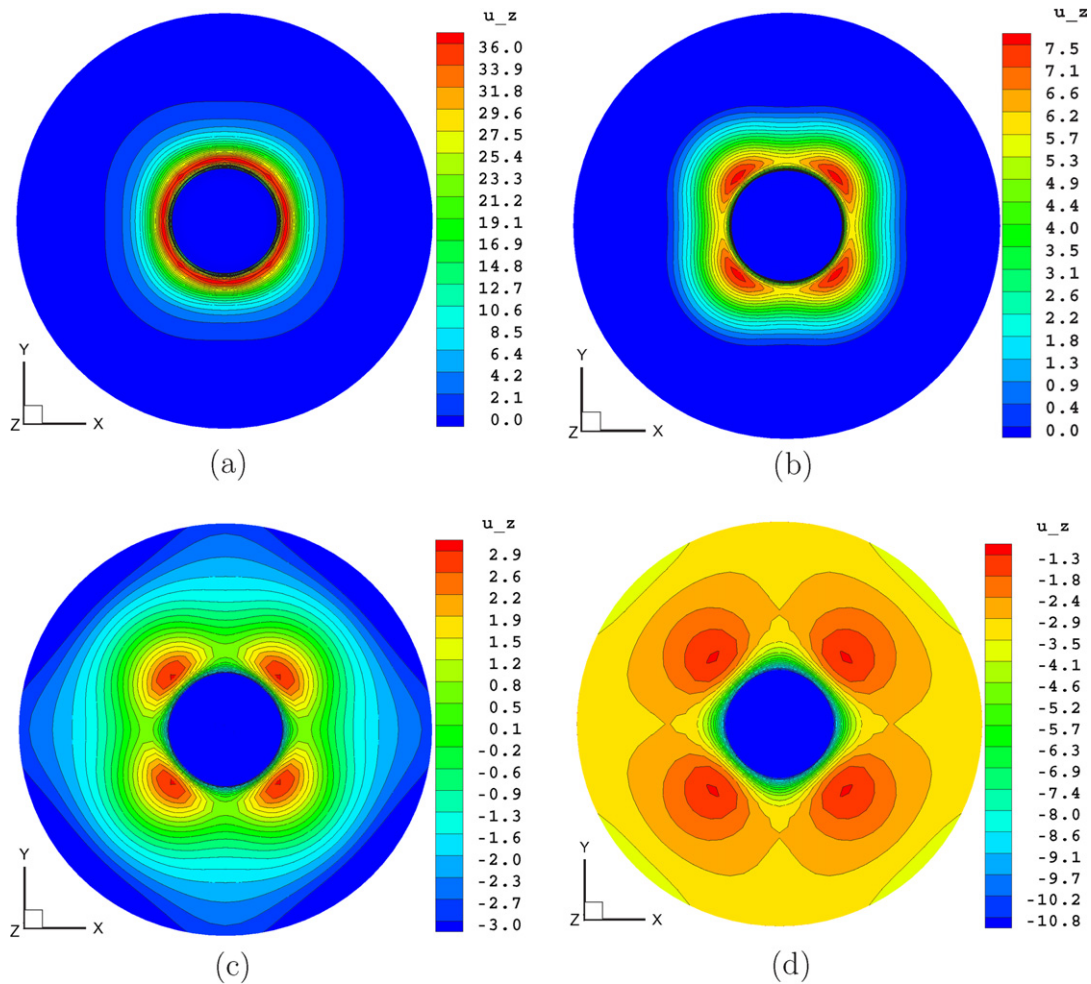

Fig. 5. Finite element analysis: isolines of height, u_z [µm], for hardening moduli $k = 0; 5; 10; 20$ GPa labelled with (a), (b), (c), (d). Pile-up for $u_z > 0$ µm, sink-in for $u_z < 0$ µm. In the coordinate systems, x-, y-axes represent [1 0 0], [0 1 0] directions.

in the sense that emerging hillocks are forced to dive into the crater. To study the two trends in detail, a quantitative comparison of pile-up for different values of the hardening rate is in order. For $k = 5$ GPa four distinct hillocks in $\langle 110 \rangle$ directions emerge close to the indentation crater, Fig. 5(b). Compared to the case of zero hardening, the deformation pattern still is throughout pile-up, but the absolute height of the peaks has considerably decreased, from maximum value max $u_z = 37$ μm for $k = 0$ GPa to max $u_z = 8$ μm for $k = 5$ GPa. With an increasing hardening rate, from $k = 5$ GPa to $k = 10$ GPa, an additional separation and elevation of the $\langle 110 \rangle$ hillocks is induced. Although the maximum values of out-of-plane displacements decrease from $u_z = 8$ μm to $u_z = 3$ μm, the relative height of the hillocks with respect to their bases increases. For $k = 10$ GPa material at the inside of the crater slightly sinks in at $\langle 100 \rangle$ directions leading to corresponding corners, see Fig. 5(c).

Fig. 5(d) displays the remaining deformation pattern after unloading for $k = 20$ GPa. The isolines of height indicate throughout sink-in which is strongest in $\langle 100 \rangle$ directions, where sink-in corners form a squared shape of the circle.

4. Conclusions

(i) The indentation pattern of the experiment with a geometrically isotropic spherical indenter reflects the material's cubic symmetry. In the (001) oriented surface, pile-up patterns emerge at $\langle 110 \rangle$ directions and therefore show four-fold symmetry. Pile-up leads to locally extended contact zones. They appear as *corners* in the circular indent and – when seen from the top – as a *squaring of the circle*.

(ii) The experimental pile-up topography and the slip-traces at the surface can be kinematically explained in terms of the pronounced out-of-plane displacement of material along the intersection vectors between the crystallographic $\{111\}\langle 110 \rangle$ slip directions and the indented (001) surface. The conclusion is, that plastic slip in octahedral planes instead of cubic planes is predominant.

(iii) The proposed phenomenological model of orthotropic elasto-plasticity proves within the finite element analysis its predictive capacity to describe the pattern formation. Simulation and experiment are in qualitative agreement.

(iv) The simulations suggest, that the rate of isotropic hardening is the knife to shape the cubic symmetry in the deformation patterns, where this observation

is overlapped by the well-known effect of isotropic hardening to cause global sink-in: a roughly isotropic pile-up formation for a zero hardening rate is continuously separated into $\langle 110 \rangle$ hillocks and increasingly diving down $\langle 100 \rangle$ valleys. Those valleys, while sinking in below the initial surface level for a very large hardening rate, lead to sharp corners in the indentation shape. Experiments with samples of the same material but with different hardening rates are necessary to validate this prediction.

References

[1] Y.T. Cheng, T. Page, G.M. Pharr, M.V. Swain, K.J. Wahl (Eds.), J. Mater. Res. 19 (2004) 1–395.
[2] D. Tabor, Hardness of Metals, Clarendon, Oxford, 1951.
[3] A. Bolshakov, G.M. Pharr, J. Mater. Res. 13 (1998) 1049–1058.
[4] A.E. Giannakopoulos, S. Suresh, Scr. Mater. 40 (1999) 1191–1198.
[5] J. Alcalá, A.C. Barone, M. Anglada, Acta Mater. 48 (2000) 3451–3464.
[6] K. Wintrich, Schädigungsverhalten der einkristallinen Superlegierung CMSX-4 bei Hochtemperaturbelastung (in German), Ph.D. thesis, TU Darmstadt, 2004.
[7] L.D. Dyer, Trans. ASM 58 (1965) 620–644.
[8] M. Hollatz, M. Bobeth, W. Pompe, V. Marx, Acta Mater. 44 (1996) 4149–4159.
[9] Y. Wang, D. Raabe, C. Klüber, F. Roters, Acta Mater. 52 (2004) 2229–2238.
[10] B. Eidel, Anisotropic inelasticity – Modelling, simulation, validation, Ph.D. thesis, TU Darmstadt, Shaker, Aachen, 2005.
[11] E. Kröner, Arch. Rat. Mech. Anal. 4 (1960) 273–334.
[12] E.H. Lee, J. Appl. Mech. 36 (1969) 1–6.
[13] J. Mandel, in: CISM Lecture Notes No. 97, Springer, Udine, 1971.
[14] Y.F. Dafalias, Int. J. Plast. 14 (1998) 909–931.
[15] Ch. Tsakmakis, Int. J. Plast. 20 (2004) 167–198.
[16] J. Lubliner, Plasticity Theory, first ed., Macmillan, New York, 1990.
[17] J. Betten, in: J.P. Boehler (Ed.), Applications of tensor functions in solid mechanics, CISM Course No. 292, Springer, Heidelberg, 1987, pp. 227–250.
[18] J.P. Boehler, in: J.P. Boehler (Ed.), Applications of tensor functions in solid mechanics, CISM Course No. 292, Springer, Heidelberg, 1987, pp. 13–30.
[19] A.J.M. Spencer, in: A.C. Eringen (Ed.), Continuum Physics, 1, Academic Press, New York, 1971, pp. 239–353.
[20] S. Klinkel, Theorie und Numerik eines Volumen-Schalen-Elementes bei finiten elastischen und plastischen Verzerrungen (in German), Ph.D. thesis, Universität Karlsruhe (TH), 2000.